

1 **Sound Velocities of Iron-Nickel (Fe₉₀Ni₁₀) Alloy up to 8 GPa and 773 K: The Effect of**
2 **Nickel on the Elastic Properties of bcc-Iron at High P-T**

3

4 **Siheng Wang^{1,*}, Nao Cai^{2,†}, Xintong Qi², Sibo Chen¹, and Baosheng Li^{1,2}**

5

6 ¹Department of Geosciences, Stony Brook University, Stony Brook, NY 11794, USA

7 ²Mineral Physics Institute, Stony Brook University, Stony Brook, NY 11794, USA

8

9 *Corresponding author: Siheng Wang (siheng.wang@stonybrook.edu), Department of
10 Geosciences, Stony Brook University, Stony Brook, NY 11794, USA

11 †Current addresses: College of Earth and Planetary Sciences, University of Chinese Academy of
12 Sciences, Beijing, China.

13

14 **Abstract**

15 Sound velocities of iron and iron-based alloys at high pressure and high temperature are crucial
16 for understanding the composition and structure of Earth's and other telluric planetary cores. In
17 this study, we performed ultrasonic interferometric measurements of both compressional (V_P)
18 and shear (V_S) velocities on a polycrystalline body-centered-cubic (bcc)-Fe₉₀Ni₁₀ up to 8 GPa
19 and 773 K. The elastic moduli and their pressure and temperature derivatives are derived from
20 least square fits to third-order finite strain equations, yielding $K_{S0} = 154.2(8)$ GPa, $G_0 = 73.2(2)$
21 GPa, $K_{S0}' = 4.6(2)$, $G_0' = 1.5(1)$, $\partial K_S / \partial T = -0.028(1)$ GPa/K, and $\partial G / \partial T = -0.023(1)$ GPa/K. A
22 comparison with literature data on bcc-Fe suggests the nickel content not only decreases both P
23 and S wave velocities but also weakens the temperature effects on the elastic moduli of Fe-Ni
24 alloys.

25

26 **Key words:** Fe-Ni alloy; sound velocity; high pressure and high temperature; ultrasonic
27 interferometry

28

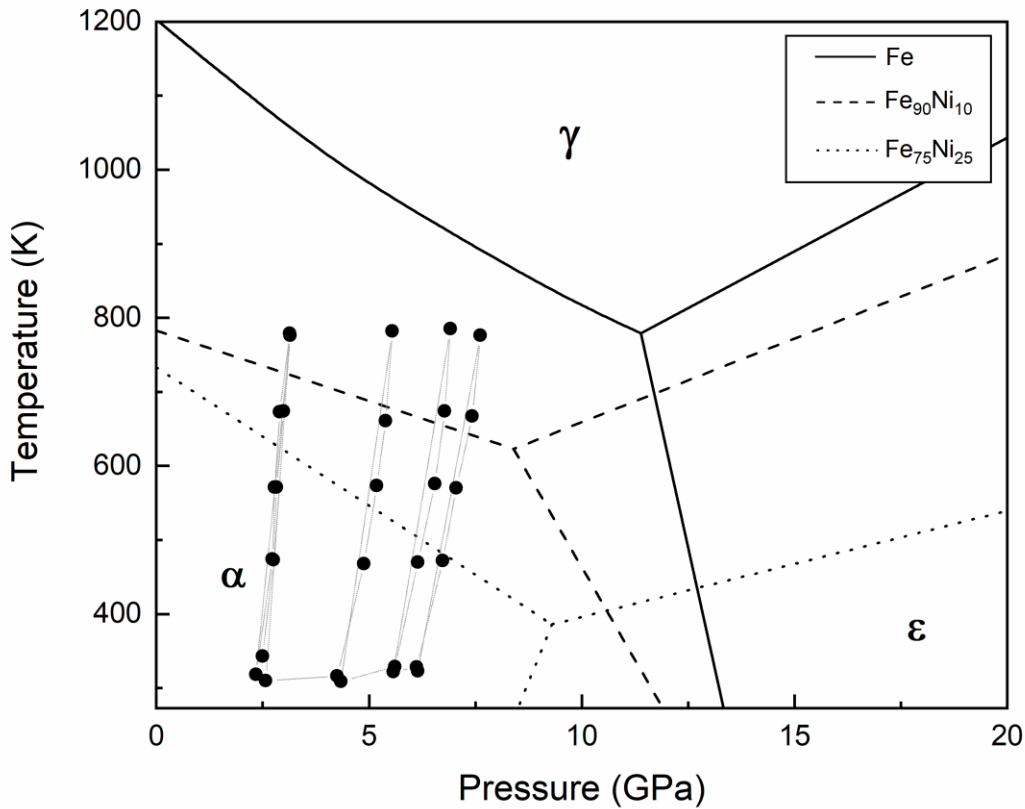
29 **1. Introduction**

30 Understanding the nature of Earth's core, which is the least accessible region of the Earth, is one
31 of the most challenging tasks in geophysical research. Seismic waves can travel inside the Earth
32 and serve as a powerful tool to probe the physical properties of Earth's interior, such as the
33 density, compressional and shear wave velocities depth profiles; see for example the Preliminary
34 Reference Earth Model [[Dziewonski and Anderson, 1981](#)]. Comparing seismic results with lab-
35 based mineral physics investigations, as well as other evidence from geochemical, and
36 cosmochemical studies, it has been widely accepted that Earth's core is composed of iron alloyed
37 with approximately 10 wt.% nickel and several percent of light elements (such as Si, O, H, S, C,
38 etc.) [e.g., [Birch, 1952](#); [1964](#); [J Li and Fei, 2003](#); [McDonough and Sun, 1995](#)]. However, direct
39 studies on the behavior and elasticity properties of iron alloys at high pressure and high
40 temperature (*HPHT*) are still scarce.

41 Iron-nickel alloys can exist in several crystallographic structures: body-centered-cubic (bcc)
42 structure (α phase), face-centered cubic (fcc) structure (γ phase), and hexagonal close-packed
43 (hcp) structure (ε phase), etc., depending on the pressure (P) and temperature (T) conditions and
44 the nickel concentration (*Figure 1*). At ambient conditions, iron crystallizes in bcc structure
45 while nickel prefers the fcc structure; when the nickel concentration exceeds ~20 wt.%, Fe-Ni
46 alloys will gradually transform from bcc to fcc structure. However, there is no conclusive
47 consensus on the phase diagram of Fe-Ni systems at high pressure and high temperature.
48 Although most experimental evidences show that Fe-Ni alloy crystallize in the hcp structure at
49 Earth's core conditions [e.g., [H K Mao et al., 1990](#); [Sakai et al., 2014](#); [Tateno et al., 2010](#);
50 [Tateno et al., 2012](#)], there are also experimental and theoretic predictions arguing that the bcc
51 structure could be a more stable phase [e.g., [Dubrovinsky et al., 2007](#); [Vocablo et al., 2003](#)].

52 With the complexity of alloying with light elements, the phase diagram is even more
 53 controversial. Thus, more information about the physical and chemical properties (such as,
 54 density, sound velocity, bulk modulus, shear modulus, anisotropy, etc.) of the different phases of
 55 the Fe-Ni alloys are needed to further constrain the composition and structure of the Earth's core.

56



57

58 *Figure 1 Phase diagram of Fe-Ni alloy system at high P-T based on the data of Huang et al., 1988; Huang et al.,*
 59 *1992. Solid dots indicate the experimental P-T conditions where the ultrasonic data were acquired in this study.*

60

61 Sound velocities of pure iron (Fe) have been experimentally accessed by ultrasonic
62 interferometry (UI), inelastic X-ray scattering (IXS), nuclear resonant inelastic X-ray scattering
63 (NRIXS), and laser pulses (LP), etc.] at room temperature [e.g., [Chigarev et al., 2008](#); [Decremps](#)
64 [et al., 2014](#); [Fiquet et al., 2001](#); [Gleason et al., 2013](#); [H K Mao et al., 1998](#); [Murphy et al., 2013](#)]
65 and high temperature [e.g., [Antonangeli et al., 2012](#); [Lin et al., 2005](#); [Liu et al., 2014](#); [Z Mao et](#)
66 [al., 2012](#); [Ohtani et al., 2013](#); [Shibasaki et al., 2016](#)]. In contrast, experimental studies on the
67 sound velocity of iron-nickel (Fe-Ni) alloys are still limited [[Kantor et al., 2007](#); [Lin et al., 2003](#);
68 [Morrison et al., 2019](#); [Wakamatsu et al., 2018](#)], especially for the shear properties under
69 simultaneous high pressure and high temperature conditions.

70 In the present study, we have carried out ultrasonic interferometric (UI) measurements on a
71 polycrystalline bcc-Fe₉₀Ni₁₀ sample at simultaneous pressure and temperature conditions.
72 Compared to other sound velocity measurement techniques, UI in large volume apparatus
73 embeds the advantages of stable and uniform heating of sample and direct measurement of both
74 P and S wave velocities simultaneously. We applied a third-order finite strain approach for data
75 analysis; the resultant compressional and shear velocities as well as the bulk and shear moduli
76 for bcc-Fe₉₀Ni₁₀ are compared with those for pure iron to evaluate the effects of nickel content on
77 the elastic properties of Fe-Ni alloys.

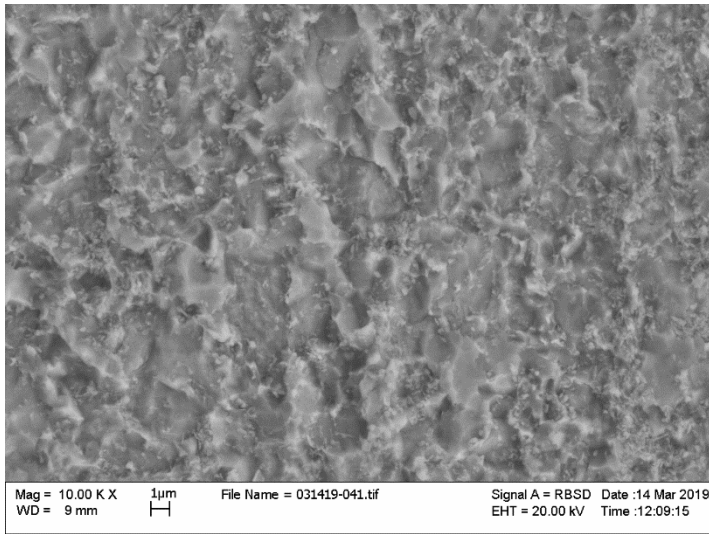
78

79 **2. Experimental methods**

80 The polycrystalline sample of Fe₉₀Ni₁₀ (10 wt.% Nickel) was a cylindrical disk cut from a rod
81 purchased from Princeton Scientific Cooperation. Before the ultrasonic measurements, the
82 sample was annealed at 3 GPa, 773 K. Scanning electron microscope (SEM) analysis was

83 conducted on the recovered sample and the results (Figure 2) indicated that the sample was
84 homogenous with an average grain size less than 1 μm . There were no detectable oxygen
85 observed in the Energy-dispersive X-ray spectroscopy (EDS), suggesting that no oxidation
86 reactions occurred during the high temperature annealing process.

87 To optimize the acoustic signals in the ultrasonic measurement, both sides of the sample were
88 polished using diamond lapping film to 1 μm . The final dimensions of the polished sample were
89 0.930(2) mm in length and 2.010(2) mm in diameter, with a bulk density of 7.95(3) g/cm^3 , as
90 obtained by the Archimedes' method.



92 *Figure 2 Scanning electron microscope image of sample after high temperature annealing.*

93

94 High pressure and high temperature ultrasonic measurements were performed to about 8 GPa,
95 773 K in a 2000-ton uniaxial split-cylinder apparatus (USCA-2000) in the High-Pressure Lab at
96 Stony Brook University. A sketch of the 14/8 cell assembly used in this study is shown in Figure
97 3. A dual mode LiNbO_3 transducer (10° Y-cut) was used to generate and receive both the

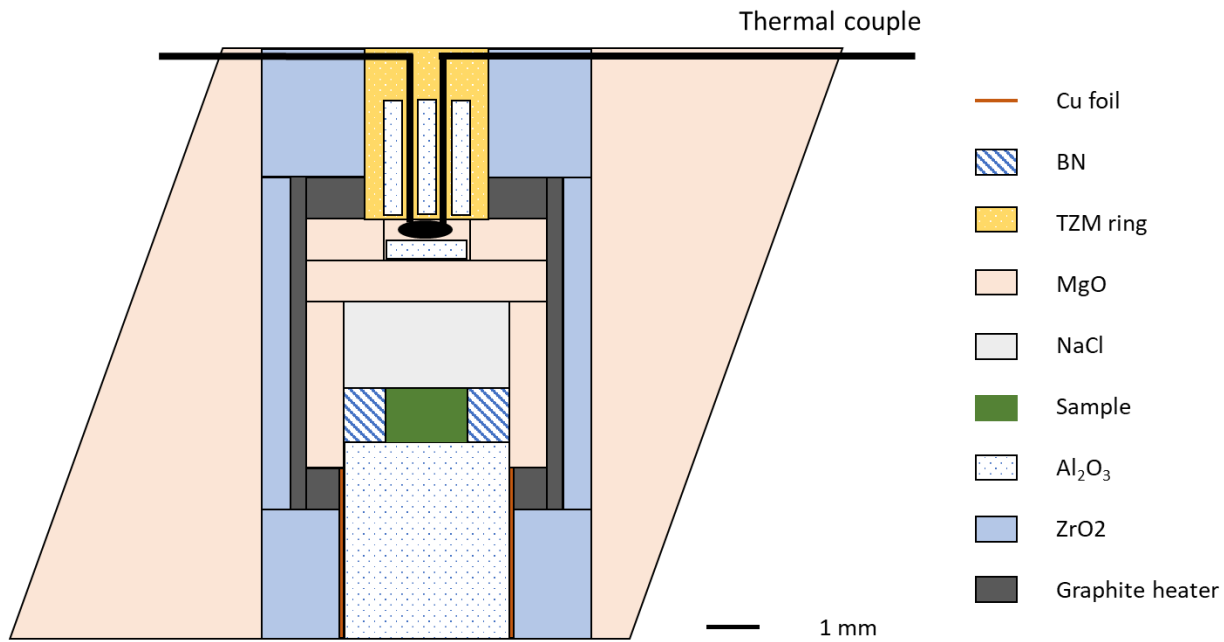
98 compressional (P) wave and shear (S) wave simultaneously (50 MHz resonant frequency for P
99 waves and 30 MHz for S waves). A dense alumina rod was placed on the top of the sample and
100 served as the acoustic buffer rod. Due to the low yield strength of NaCl at high temperatures, a
101 disk of NaCl was placed at the back of the sample to provide a pseudo-hydrostatic environment
102 during the experiment. The high temperature environment was generated by a graphite heater
103 and monitored by W/Re3%-W/Re26% type-C thermocouples, with the junction immediately
104 next to the sample near the center of the cell. The temperature measurement uncertainty in
105 current experiment is approximately ± 10 K. P and S wave travel times were acquired using the
106 transfer function technique and analyzed using the pulse echo overlap (PEO) method by
107 overlapping the buffer rod and sample echoes (Fig. 4). Details about the transfer function
108 technique for data acquisition and processing have been discussed elsewhere [[B Li et al., 2004](#); [B
109 Li et al., 2002](#)]. Cell pressures were calculated from the shear wave travel times of the alumina
110 buffer rod using the pressure scale at high temperature by equation:

$$P = 242.5(9) \times (1 - t_s/t_{s0}) + 0.01099(5) \times (T - T_0) \#(1.)$$

111 where P is cell pressure, t_s is the S wave travel time of the buffer rod, and t_{s0} is the S wave travel
112 time at ambient conditions [[for further details of the use of alumina as a pressure marker, see
113 Wang et al., 2015](#)]. The pressure uncertainty is estimated to be around ± 0.2 GPa in current study.
114 The experimental P - T path is shown in the [Figure 1](#), superimposed with the previously
115 determined phase diagram from the diamond anvil cell [[Huang et al., 1988](#); [Huang et al., 1992](#)].
116 The sample was first compressed at room temperature to a maximum pressure of ~ 8 GPa,
117 followed by heating to a peak temperature of 773 K to release the deviatoric stress in the cell,
118 then the ultrasonic data were collected at 100 K intervals along cooling paths to room

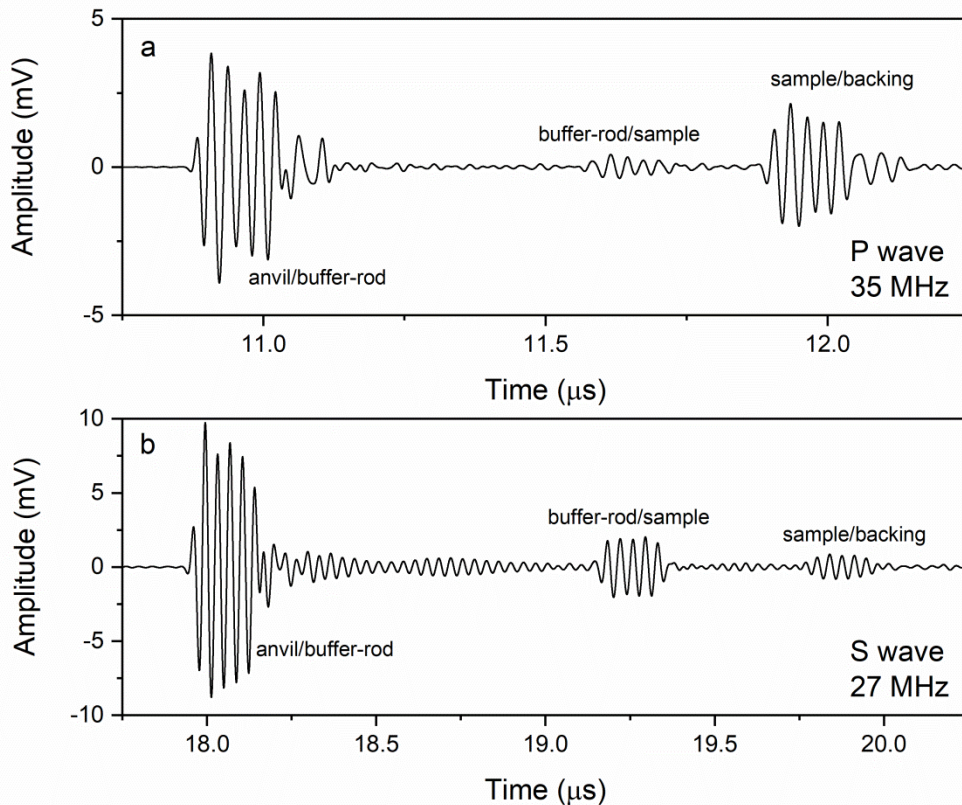
119 temperature while the sample was under nearly hydrostatic environment [[B Li et al., 2001](#)].
120 Multiple heating and cooling cycles were performed during decompression to provide a dense
121 coverage of experimental data in P-T space. The P and S wave travel times were obtained at 35
122 and 27 MHz, respectively, in this study, to maximize the signal-to-noise ratio.

123



124

125 *Figure 3 Sketch of the cell assembly used in current study for ultrasonic measurement.*



126

127 *Figure 4 Signal example of (a) P wave and (b) S wave obtained at 7.6 GPa and 776 K.*

128

129 **3. Data analyses**

130 After the experiment, the sample length and diameter were 0.926(2) mm and 2.010(5) mm
 131 respectively, indicating that, within 0.4% uncertainty, the sample can be considered to have
 132 undergone elastic compression under pseudo-hydrostatic conditions during the entire course of
 133 the experiment. As indicated by the P and S wave signals obtained at 7.6 GPa and 776 K in
 134 Figure 4, the reflections from the front (buffer rod/sample) and rear (sample/backing) surfaces
 135 are highly distinguishable from the background, providing a reliable measurements of travel
 136 times with 0.1-0.6% in precision.

137 The travel time results at all experimental conditions from this study are summarized in **Table 1**.
 138 As shown in previous studies, velocities (V_p and V_s), and elastic moduli (K_s and G) as well as
 139 their pressure and temperature derivatives (K_s , G , K_s' , G' , $\partial K_s / \partial T$, and $\partial G / \partial T$) can be obtained
 140 by a third-order finite strain approach [[Davies and Dziewonski, 1975](#); [B Li and Zhang, 2005](#)].
 141 First, because the sample has undergone nearly hydrostatic deformation during cooling along
 142 decompression the experiment, it is reasonable to assume that density (ρ), volume (V), and
 143 length (l) have the following relationships:

$$\frac{\rho}{\rho_0} = \frac{V_0}{V} = \left(\frac{l_0}{l}\right)^3 \#(2.)$$

144 The elastic properties at high pressure and temperature can be calculated through the sound
 145 velocities $V_{(P,S)} = \frac{2l}{2t_{(P,S)}}$ and densities ρ by the relationships $K_s = \rho(V_p^2 - \frac{4}{3}V_s^2)$ and $G = \rho V_s^2$
 146 for the bulk and shear modulus, respectively. Under adiabatic compression, the finite strain
 147 equations are expressed as the following:

$$\rho V_p^2 = (1 - 2\varepsilon)^{\frac{5}{2}}(L_1 + L_2\varepsilon) \#(3.)$$

$$\rho V_s^2 = (1 - 2\varepsilon)^{\frac{5}{2}}(M_1 + M_2\varepsilon) \#(4.)$$

$$K_{S(0,T)} = L_1 - \frac{4}{3}M_1 \#(5.)$$

$$G_{(0,T)} = M_1 \#(6.)$$

$$K'_{S(0,T)} = \frac{5L_1 - L_2}{3K_{S(0,T)}} - \frac{4G'_{(0,T)}}{3} \#(7.)$$

$$G'_{(0,T)} = \frac{5M_1 - M_2}{3K_{S(0,T)}} \#(8.)$$

148 where the subscript (P,T) indicates values at the pressure P and adiabatic foot temperature T , and
 149 the Eulerian strain $\varepsilon = \frac{1}{2} \left[1 - \left(\frac{\rho_{(0,T)}}{\rho_{(0,T_0)}} \right)^{2/3} \right]$. All temperatures reached in the entire experiment are
 150 assumed to be raised along separate adiabats from different foot temperatures T_0 . Thus, the
 151 adiabatic foot temperature for each data point as well as the corresponding density and elastic
 152 properties can be extracted through the following equations:

$$\left(\frac{\partial T}{\partial P} \right)_S = \frac{\gamma T}{K_S} \#(9.)$$

$$\rho_{(0,T)} = \rho_{(0,T_0)} e^{-\int \alpha dT} \#(10.)$$

$$K_{S(0,T)} = K_{S(0,T_0)} + (T - T_0) \left(\frac{\partial K_S}{\partial T} \right)_P \#(11.)$$

$$G_{(0,T)} = G_{(0,T_0)} + (T - T_0) \left(\frac{\partial G}{\partial T} \right)_P \#(12.)$$

$$K'_{SS(0,T)} = K'_{SS(0,T_0)} + (T - T_0) \left(\frac{\partial^2 K_S}{\partial P \partial T} \right)_P + \left(\frac{\partial K_S}{\partial T} \right)_P \frac{\gamma T}{K_S} \#(13.)$$

$$G'_{S(0,T)} = G'_{S(0,T_0)} + (T - T_0) \left(\frac{\partial^2 G}{\partial P \partial T} \right)_P + \left(\frac{\partial G}{\partial T} \right)_P \frac{\gamma T}{K_S} \#(14.)$$

$$P = -(1 - 2\varepsilon)^{5/2} \left(3K_{S(0,T_0)}\varepsilon + \frac{1}{2} (36K_{S(0,T_0)} - 9K_{S(0,T_0)}K'_{SS(0,T_0)})\varepsilon^2 \right) \#(15.)$$

153 The sample lengths, as well as the thermoelastic properties K_S , G , K'_S , G' , $\partial K_S / \partial T$, $\partial G / \partial T$ at
 154 ambient conditions, were refined using a least-square fit by minimizing the difference between
 155 the observed compressional and shear velocities ($V_{(P,S)} = \frac{2l}{2t_{(P,S)}}$) and pressures (P from [eq.(1)]
 156 with those calculated by finite strain theory [eqs. (3), (4), and (15)]. More details about the data
 157

158 analysis procedures can be found elsewhere [[B Li and Zhang, 2005](#)]. In the P - T range of the
159 current experiment, the thermal expansivity α was assumed to be a constant value of 4.67×10^{-5}
160 [[Zhang and Guyot, 1999](#)]; the Grüneisen parameter γ was constrained by the assumption of $p\gamma =$
161 constant with $\gamma_0 = 1.65$ [[Poirier, 2000](#); [Quarenici and Mularcja, 1988](#)]; cross derivatives
162 $(\partial^2 K_S / \partial P \partial T)_P$ and $(\partial^2 G / \partial P \partial T)_P$ were assumed to be zero in the current P - T range. The
163 minimization usually takes only a few iterations to achieve convergence, and the results for the
164 elastic properties are shown in **Table 2**.

165

Table 1 Experimental data of bcc- $Fe_{90}Ni_{10}$

<i>P</i> (GPa)	<i>T</i> (K)	$2t_P$ (μs)	$2t_S$ (μs)	Length (mm)	ρ (g/cm ³)	V_P (km/s)	V_S (km/s)	K_S (GPa)	<i>G</i> (GPa)
6.2	323	0.3080(2)	0.5816(28)	0.9148	8.246	5.94(6)	3.15(3)	182.2(33)	81.6(11)
7.6	776	0.3188(4)	0.6188(18)	0.9174	8.176	5.76(6)	2.97(3)	175.0(30)	71.9(8)
7.4	667	0.3150(4)	0.6060(4)	0.9165	8.200	5.82(6)	3.02(3)	177.6(30)	75.0(8)
7.1	570	0.3124(4)	0.5968(8)	0.9160	8.212	5.86(6)	3.07(3)	179.2(31)	77.4(8)
6.7	472	0.3104(2)	0.5868(22)	0.9155	8.228	5.90(6)	3.12(3)	179.5(32)	80.1(10)
6.1	328	0.3080(4)	0.5810(28)	0.9149	8.243	5.94(6)	3.15(3)	181.9(34)	81.8(11)
5.6	322	0.3092(4)	0.5828(22)	0.9157	8.220	5.92(6)	3.14(3)	180.2(33)	81.2(10)
6.9	785	0.3210(12)	0.6208(16)	0.9188	8.140	5.72(6)	2.96(3)	171.6(35)	71.3(8)
6.8	674	0.3172(6)	0.6096(8)	0.9177	8.167	5.79(6)	3.01(3)	174.7(31)	74.0(8)
6.6	576	0.3146(8)	0.5990(10)	0.9170	8.186	5.83(6)	3.06(3)	175.9(33)	76.7(8)
6.2	470	0.3120(2)	0.5900(10)	0.9165	8.201	5.87(6)	3.11(3)	177.5(31)	79.1(8)
5.6	329	0.3098(2)	0.5826(28)	0.9158	8.219	5.91(6)	3.14(3)	179.0(33)	81.2(11)
4.3	309	0.3140(4)	0.5864(12)	0.9178	8.165	5.85(6)	3.13(3)	172.4(31)	80.0(9)
5.6	782	0.3256(2)	0.6244(6)	0.9213	8.073	5.66(6)	2.95(3)	164.8(28)	70.3(7)
5.4	661	0.3214(2)	0.6130(4)	0.9201	8.103	5.73(6)	3.00(3)	168.3(29)	73.0(7)
5.2	573	0.3192(2)	0.6050(2)	0.9195	8.121	5.76(6)	3.04(3)	169.5(29)	75.0(8)
4.9	468	0.3172(2)	0.5984(2)	0.9188	8.139	5.79(6)	3.07(3)	170.8(29)	76.7(8)
4.3	316	0.3150(2)	0.5878(10)	0.9181	8.158	5.83(6)	3.12(3)	171.0(30)	79.6(8)
2.6	310	0.3206(4)	0.6010(18)	0.9211	8.077	5.75(6)	3.07(3)	165.5(30)	75.9(9)
3.1	779	0.3336(2)	0.6406(8)	0.9260	7.950	5.55(6)	2.89(3)	156.4(26)	66.4(7)
2.9	673	0.3300(2)	0.6268(20)	0.9251	7.974	5.61(6)	2.95(3)	158.0(28)	69.5(8)
2.8	571	0.3266(4)	0.6188(26)	0.9240	8.002	5.66(6)	2.99(3)	161.1(29)	71.4(9)
2.7	474	0.3244(4)	0.6134(38)	0.9229	8.030	5.69(6)	3.01(3)	163.0(31)	72.7(12)
2.3	318	0.3218(2)	0.6028(14)	0.9217	8.062	5.73(6)	3.06(3)	164.0(29)	75.4(8)
3.2	776	0.3334(2)	0.6352(16)	0.9259	7.952	5.55(6)	2.92(3)	155.2(27)	67.6(8)
3.0	674	0.3302(2)	0.6244(4)	0.9249	7.978	5.60(6)	2.96(3)	157.0(27)	70.0(7)
2.8	571	0.3270(2)	0.6188(22)	0.9239	8.003	5.65(6)	2.99(3)	160.4(28)	71.4(9)
2.8	473	0.3246(2)	0.6114(4)	0.9229	8.031	5.69(6)	3.02(3)	162.1(28)	73.2(7)
2.5	343	0.3226(2)	0.6050(10)	0.9218	8.060	5.71(6)	3.05(3)	163.4(29)	74.8(8)

Notes: The uncertainty of length calculated in this study is approximately $\pm 1\%$.

168 **Table 2** Comparison of thermoelastic properties of Fe and Fe-Ni alloys

169

Reference			P range (GPa)	T range (K)	K_{S0} (GPa)	$\partial K_{S0}/\partial P$ (GPa/K)	$\partial K_{S0}/\partial T$ (GPa/K)	G_0 (GPa)	$\partial G_0/\partial P$ (GPa/K)	$\partial G_0/\partial T$ (GPa/K)	K_{T0} (GPa)	$\partial K_{T0}/\partial P$ (GPa/K)	$\partial K_{T0}/\partial T$ (GPa/K)	EOS	Notes
This study	bcc	Fe ₉₀ Ni ₁₀	~8	~773 ~673	154.2(8) 153.8(7)	4.6(2) 4.7(2)	-0.028(1) -0.027(2)	73.2(2) 72.7(2)	1.5(1) 1.6(1)	-0.023(1) -0.022(1)	— —	— —	— —	3rd Finite strain	Ultrasonic, adiabatic
Shibasaki et al. (2016)	bcc	Fe	~6.3	~800	163.2(15)	6.75(33)	-0.038(3)	81.4(6)	1.66(14)	-0.029(1)	— —	— —	— —	Polynomial	Ultrasonic, adiabatic
Adams et al. (2006)	bcc	Fe	0	3-500	166.2	—	-0.029	81.5	—	-0.025	— —	— —	— —	—	Ultrasonic, adiabatic
Isaak and Masuda (1995)	bcc	Fe	0	~800	165.7	—	-0.046	82	—	-0.034	— —	— —	— —	—	Ultrasonic, adiabatic
Dever (1972)	bcc	Fe	0	~773	167.8	—	-0.035	82	—	-0.029	— —	— —	— —	—	Ultrasonic, adiabatic
Zhang and Guyot (1999)	bcc	Fe	~9	~773	—	—	—	—	—	155(2)	5.3*	-0.049(6)	3rd Birch Murnaghan	XRD, isothermal	
Huang et al. (1987)	bcc	Fe	~12	~723	—	—	—	—	—	171(8)	4*	-0.010(16)	Birch Murnaghan	XRD, isothermal	
Takahashi et al. (1968)	bcc	Fe	~15	300	—	—	—	—	—	162(5)	5.5(8)	—	Murnaghan	XRD, isothermal	
	bcc	Fe ₉₅ Ni ₅	~16	300	—	—	—	—	—	155(10)	4.2(8)	—			
	bcc	Fe ₉₀ Ni ₁₀	~17	300	—	—	—	—	—	155(10)	5.7(8)	—			
Morrison et al. (2018)	bcc	Fe ₉₁ Ni ₉	~15	300	—	—	—	—	—	146.8(31)	6.39(64)	—	3rd Birch Murnaghan	XRD, isothermal	
Kantor et al. (2007)	fcc	Fe ₇₈ Ni ₂₂	~72	300	—	—	—	—	—	161(1)	4.97(1)	—	3rd Birch Murnaghan	XRD, isothermal	
Huang et al. (1992)	fcc	Fe ₇₀ Ni ₃₀	~48	300	—	—	—	—	—	160(15)	4*	—	Birch Murnaghan	XRD, isothermal	

Notes:

*: fixed value

170 WHY dK/dT from Zhang and Guyot (1999) and Huang (1987) are not included here?

171

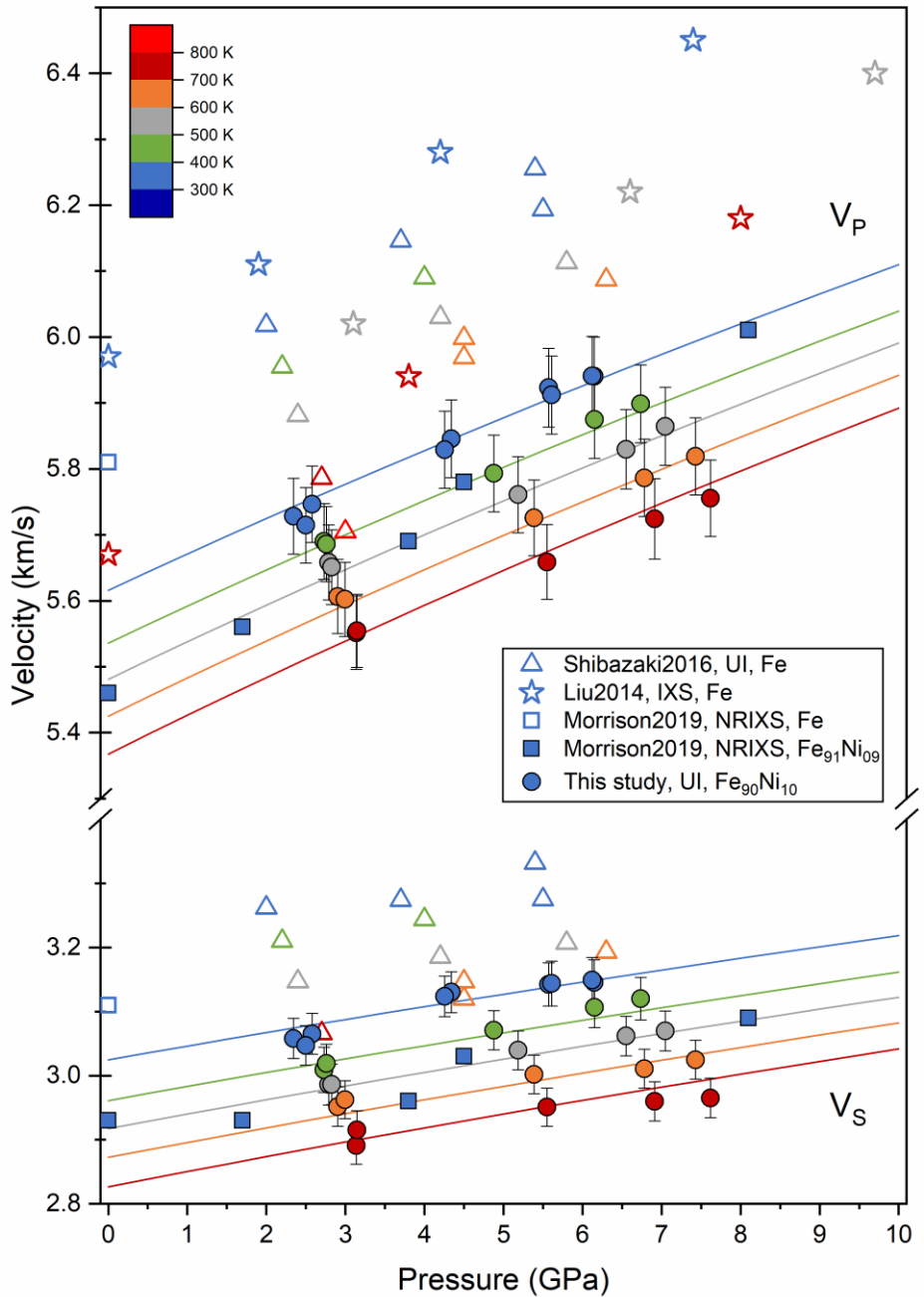
172 **4. Results and discussion**

173 According to Figure 1, some of our experimental data were collected close to the bcc-fcc
 174 boundary or within the stability field of the fcc phase of Fe90Ni10. A close examination of the
 175 recorded waveforms as well as the subsequent analysis of P and S wave travel times did not
 176 suggest a phase transition to fcc phase at these conditions. This was further tested by performing
 177 a separate fit without the data at 773 K. As indicated by the results shown in Table 2, within the
 178 uncertainty, the inclusion of the data at 773 K has an insignificant effect on the fitting results,
 179 and can be reliably treated as the representative values for the bcc phase.

180 The compressional and shear wave velocities data obtained in this study are compared in Figure
 181 5 with those from ultrasonic measurements [Shibasaki et al., 2016] and an IXS study on bcc-Fe
 182 [Liu et al., 2014], as well as data from NRIXS studies on both bcc-Fe and bcc-Fe₉₁Ni₉

183 [Morrison *et al.*, 2019]. At room temperature, the velocities of both P and S waves for bcc-
184 Fe₉₀Ni₁₀ are consistently lower than pure Fe from *Shibazaki et al. [2016]* by 5% and 6%,
185 respectively, which is in good agreement with the 5-6% (Check?)velocity depression observed in
186 NRIXS studies on Fe-Ni alloys with 0 and 9 at.% nickel [Morrison *et al.*, 2019]. However, the
187 absolute values for both P and S waves from NRIXS are systematically lower than those from
188 other techniques (UI, IXS), which could be attributed to the fact that NRIXS bases on the Debye
189 model to analyze the data instead of measuring the sound velocity directly. Comparing to those
190 for bcc-Fe from *Shibazaki et al. [2016]*, V_P of bcc-Fe₉₀Ni₁₀ from current study exhibits a slower
191 rate of increase with pressure [$\sim 5.1 \times 10^{-2}$ km/s/GPa versus(vs.) 6.9×10^{-2} km/s/GPa for Fe₉₀Ni₁₀
192 and Fe, respectively] while V_S increases at a relatively similar rate ($\sim 2.1 \times 10^{-2}$ km/s/GPa vs.
193 2.0×10^{-2} km/s/GPa for Fe₉₀Ni₁₀ and Fe, respectively).

194 With increasing temperature, both V_P and V_S decrease within the entire P - T range of the current
195 experiment with a larger reduction in V_S than V_P . For example, at ~ 3 GPa, the depression in V_P
196 and V_S from 300 K to 800 K are 4%, 7% for Fe₉₀Ni₁₀ and 6%, 8% for pure Fe, respectively. The
197 compressional velocity (V_P) decrease from 300 to 700 K reported by *Liu et al. [2014]* is about
198 5%, which is larger than the 4% for bcc-Fe₉₀Ni₁₀ observed in current study. In addition, nonlinear
199 elastic anomalies indicative of a magnetic transition at high temperature [e.g., *Dever, 1972*] were
200 not observed in the current study, which could possibly be explained by the low temperature
201 range (300-773 K) relative to the Currie temperature ($T_c = ????$) for FeNi10% .
202



203

204 *Figure 5 Compressional (V_p) and shear (V_s) wave velocities as a function of pressure and temperature.*
 205 *Solid lines are the finite strain fitted curves from this study. Temperature information are color coded and*
 206 *shown in legend.*

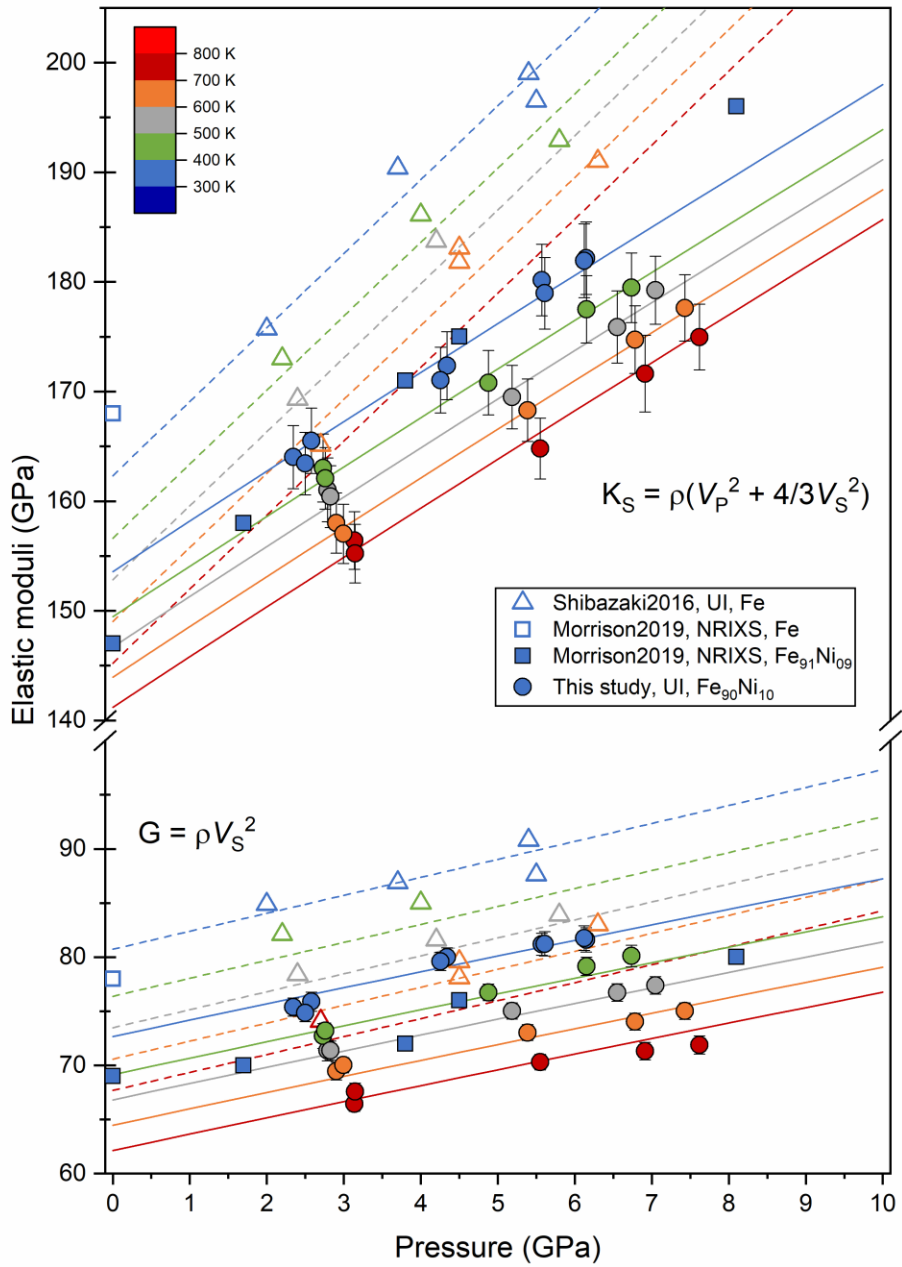
207 The adiabatic bulk modulus (K_S) and shear modulus (G) calculated in current study are plotted in
208 Figure 6 as a function of pressure and temperature. **Table 2** is a comparison of the thermoelastic
209 properties of Fe and Fe-Ni alloys obtained from this study and previous experimental studies.
210 Note in this table that our study reports for the first time the temperature dependences of the
211 elastic bulk and shear moduli ($\partial K_S / \partial T$ and $\partial G / \partial T$) of bcc-Fe₉₀Ni₁₀. Comparing with previous
212 ultrasonic studies listed in **Table 2**, the bulk and shear moduli of bcc-Fe₉₀Ni₁₀ at ambient
213 conditions [$K_{S0} = 154.2(8)$ GPa and $G_0 = 73.2(2)$ GPa] are lower than those values of bcc-Fe
214 ($K_{S0} = 165\text{--}168$ GPa and $G_0 = 81\text{--}82$ GPa) by approximately 6% and 11%, respectively [[Adams et al., 2006](#); [Dever, 1972](#); [Isaak and Masuda, 1995](#); [Shibasaki et al., 2016](#)]. The effect of nickel
215 content on bulk modulus observed in this study is consistent with previous suggestions based on
216 pressure-volume (P - V) measurements in diamond anvil cell [[Morrison et al., 2018](#); [Takahashi et al., 1968](#)].

219 It is also worthwhile to note that, comparing with pure bcc-Fe ([Shibasaki et al. \[2016\]](#), bcc-
220 Fe₉₀Ni₁₀ exhibits a weaker pressure dependence of K_S than bcc-Fe (Fig. 6), which can be
221 quantified by the pressure derivative K_S' [4.6(2) for bcc-Fe₉₀Ni₁₀ vs. 6.75(33) for pure Fe];
222 meanwhile for the shear modulus, bcc-Fe₉₀Ni₁₀ and bcc-Fe show close agreement with each
223 other in their pressure derivatives [$G_0' = 1.5(1)$ vs. 1.66(14), respectively]. These comparisons
224 are believed to reveal primarily the intrinsic difference resulted from nickel substitution in the
225 alloy, the different pressure calibration method used in the current experiments (alumina pressure
226 gauge) and those of [Shibasaki et al. \[2016\]](#) [equation of state (EOS) of MgO + hBN] may also
227 contribute, but are not considered to be an appreciable effect. Future investigations on Fe-Ni
228 alloys with different Ni contents using either of the pressure calibration method could help
229 further address this issue.

230 Besides the pressure dependence, we also investigated the effect of 10 wt.% nickel content in our
231 sample on the temperature dependence of both bulk and shear moduli. For pure bcc-Fe, high
232 temperature ultrasonic measurements have been conducted at ambient pressure [[e.g., Adams et](#)
233 [al., 2006; Dever, 1972; Isaak and Masuda, 1995](#)] and high pressure [[Shibasaki et al., 2016](#)], the
234 reported temperature dependence ranges from $-0.029 \text{ GPa/K} \sim -0.046 \text{ GPa/K}$ for the bulk
235 modulus ($\partial K_{S0}/\partial T$) and $-0.025 \text{ GPa/K} \sim -0.034 \text{ GPa/K}$ for the shear modulus ($\partial G_0/\partial T$). Our
236 results of $\partial K_{S0}/\partial T = -0.028(1) \text{ GPa/K}$ and $\partial G_0/\partial T = -0.023(1) \text{ GPa/K}$ for bcc-Fe₉₀Ni₁₀ are only
237 marginally consistent with the lowest values reported for bcc-Fe, indicating that 10 wt% nickel
238 alloying with Fe can noticeably(?) affect the temperature dependence of both bulk and shear
239 moduli.

240 The current adiabatic value of $\partial K_{S0}/\partial T = -0.028(1) \text{ GPa/K}$ can be converted to its isothermal
241 counterpart using the differentiated form of the thermodynamic identity $K_T = K_S/(1 + \alpha\gamma T)$,
242 yielding $\partial K_{T0}/\partial T = -0.038(1) \text{ GPa/K}$. Two pressure-volume-temperature (*P-V-T*) investigations
243 have reported $\partial K_{T0}/\partial T$ on bcc-Fe based on X-ray diffraction (XRD) studies and the results are in
244 large discrepancy. While [[Huang et al. \[1987\]](#) reported a relatively small temperature dependence
245 [$\partial K_{T0}/\partial T = -0.010(16) \text{ GPa/K}$], [[Zhang and Guyot \[1999\]](#) provided a much larger value [$\partial K_{T0}/\partial T$
246 $= -0.049(6) \text{ GPa/K}$], which is more consistent with the current ultrasonic results. To the authors'
247 best knowledge, no *P-V-T* investigation on bcc-Fe-Ni alloy has yet been reported to provide a
248 direct comparison with the current result.

249



250

251 *Figure 6 Bulk and shear modulus as a function of pressure and temperature. Solid lines are the finite*
 252 *strain fitted curves from this study. Dashed lines are calculated from [Shibazaki et al. \[2016\]](#).*
 253 *Temperature information are color coded and shown in legend.*

254 **5. Implications**

255 The effect of nickel content on P and S wave velocities observed on bcc phase in this study is
256 roughly consistent with the previously reported results on hcp Fe-Ni alloys [[Lin et al., 2003](#);
257 [Morrison et al., 2019](#); [Wakamatsu et al., 2018](#)]. This effect could lead to a velocity decrease as
258 large as $\Delta V_P = 0.8$ km/s at inner core boundary (ICB), as calculated by [Ohtani et al. \[2013\]](#),
259 suggesting that nickel content plays as an important factor when we modelling the velocity
260 structure of Earth's core to place constraints on its composition. Moreover, our results suggest
261 that the effect of temperature on the bulk and shear moduli of Fe-Ni alloy with 10 at% Ni is
262 likely to be lower compared to that of Fe. This means the use of temperature derivatives of Fe
263 could produce an upper bound or overestimated values for the Earth's core. In literature, [Lin et al.](#)
264 [\[2005\]](#) suggested a temperature effect of $\partial V_P / \partial T = -0.35$ km/(s· 10^3 K) and $\partial V_S / \partial T = -0.46$
265 km/(s· 10^3 K) at constant density of ~ 10.25 g/cm³ from their measurement up to 73 GPa and 1700
266 K. As it has been generally accepted that the thermal effect could be suppressed by pressure
267 effect at core conditions, thus, we may find [Ohtani et al. \[2013\]](#) gave a smaller value of $\partial V_P / \partial T =$
268 -0.12 km/(s· 10^3 K) by combing their IXS measurement up to 1100 K with theoretical calculations
269 up to 5500 K. From our measurements, we observed $\partial V_P / \partial T = -0.18(2)$ km/(s· 10^3 K) for bcc-
270 Fe₉₀Ni₁₀ at a constant density in current *P-T* range (see the velocity-density plot in Figure 7). For
271 bcc-Fe, [Shibasaki et al. \[2016\]](#) reported $\partial V_P / \partial T = -0.33(4)$ km/(s· 10^3 K) by UI and [Liu et al.](#)
272 [\[2014\]](#) reported $\partial V_P / \partial T = -0.37(3)$ km/(s· 10^3 K) by IXS in a similar *P-T* range. These values of
273 bcc-Fe are in general agreement with each other but consistently larger than the value for bcc-
274 Fe₉₀Ni₁₀, indicating the nickel content can reduce the effect of temperature on the V_P - ρ
275 relationship. If we further analog the weaker temperature effect from nickel alloying to hcp
276 phase, the $\partial V_P / \partial T$ at core conditions could be even smaller. Therefore, the nickel content caused

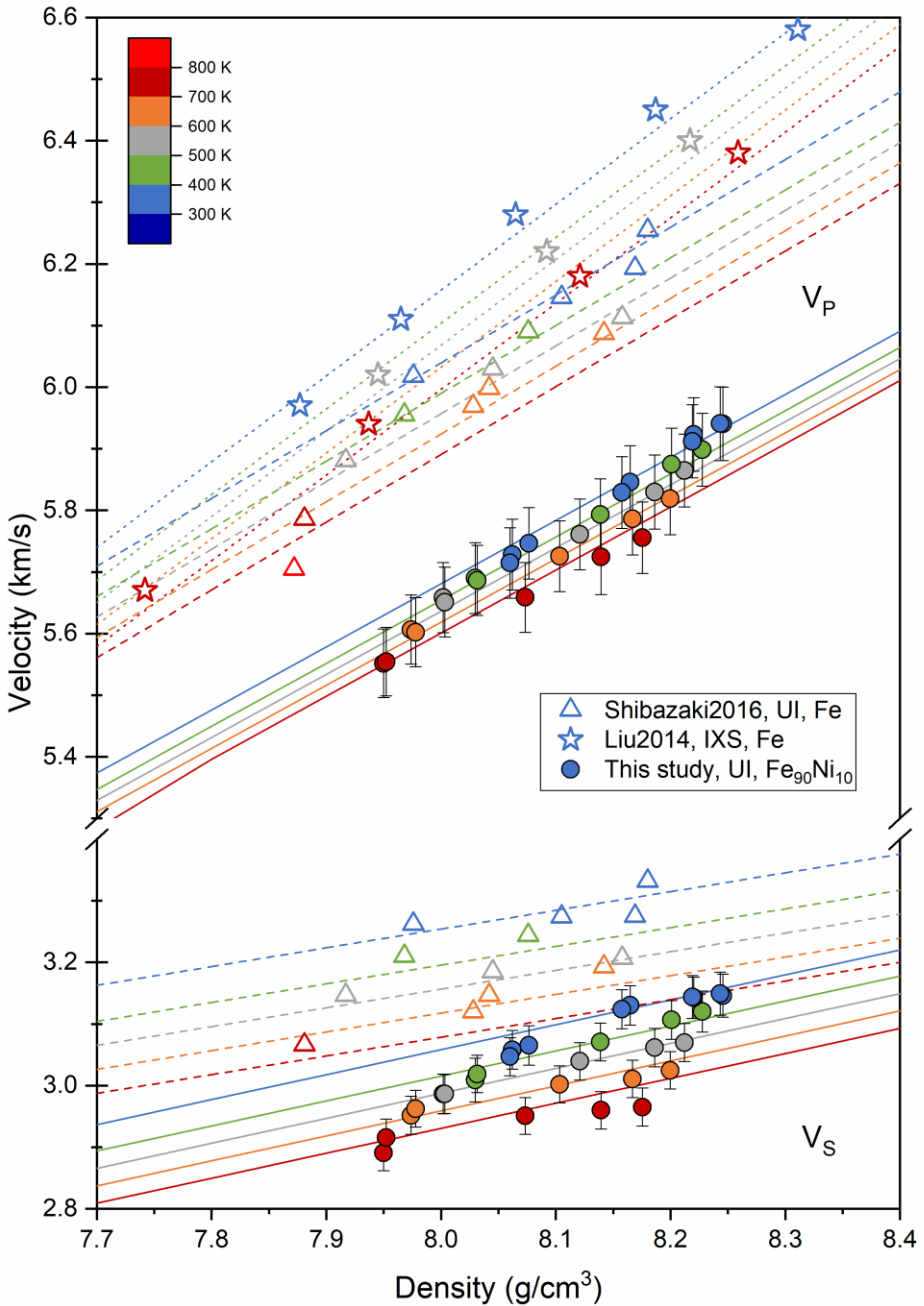
277 V_P depression at room temperature could be compensated by the weaker temperature effect at
278 core temperature. Thus, the V_P of hcp-Fe-Ni could be higher than hcp-Fe at core conditions,
279 which may require less V_P increase from alloying with light elements or even V_P decrease from
280 alloying with light elements, depending on the core temperature.

281

282 Moreover, we also observed a slightly smaller temperature effect of shear velocity in bcc-
283 Fe₉₀Ni₁₀ [$V_S/\partial T = -0.28(2)$ km/(s·10³K)] than bcc-Fe [$\partial V_S/\partial T = -0.39(3)$ km/(s·10³K)]. If this
284 effect holds true to hcp phase, the low value of $\partial V_S/\partial T$ would introduce even larger V_S of hcp-Fe-
285 Ni than previous estimations, which requires a more significant pre-melting effects [[Martorell et](#)
286 [al., 2013](#)] or other mechanism to account for the discrepancy of shear waves with the
287 seismological observations. Thus, the nickel alloying induced decrease in the temperature effect
288 needs to be further evaluated in other structures of Fe-Ni alloys in an expanded *P-T* range. Future
289 acoustic measurements of both V_P and V_S of various Fe-light elements alloys and compounds at
290 simultaneous high *P-T* conditions are also needed to provide a more comprehensive
291 understanding of the composition and thermal structure of Earth's and planetary cores.

292

293 Shorten the Implication section? We can have more discussions.



294

295 *Figure 7 Compressional (V_p) and shear (V_s) wave velocities as a function of density and temperature.*
 296 *Solid lines are the linear curves calculated from this study. Dashed lines are calculated from [Shibazaki et](#)*
 297 *[al. \[2016\]](#). Dot lines are calculated from [Liu et al. \[2014\]](#). Temperature information are color coded and*
 298 *shown in legend.*

299 **Acknowledgements**

300 The authors would like to thank Jim Quinn for assistant with SEM at Stony Brook University.

301 We also thank Robert. C. Liebermann for valuable discussions of this manuscript. This project is

302 supported by National Science Foundation (EAR-1524078) and DOE-NNSA (DE-NA0003886).

303 MPI publication number [512](#).

304

References

305 Adams, J. J., D. S. Agosta, R. G. Leisure, and H. Ledbetter (2006), Elastic constants of
306 monocrystal iron from 3 to 500 K, *Journal of Applied Physics*, 100(11), doi:
307 10.1063/1.2365714.

308 Antonangeli, D., T. Komabayashi, F. Occelli, E. Borissenko, A. Walters, G. Fiquet, and Y. Fei
309 (2012), Simultaneous sound velocity and density measurements of hcp iron up to 93GPa and
310 1100K: An experimental test of the Birch's law at high temperature, *Earth and Planetary Science
311 Letters*, 331-332, 210-214, doi: 10.1016/j.epsl.2012.03.024.

312 Birch, F. (1952), Elasticity and Constitution of the Earth Interior, *Journal of Geophysical
313 Research*, 57(2), 227-286, doi: DOI 10.1029/JZ057i002p00227.

314 Birch, F. (1964), Density and composition of the mantle and the core, *Journal of Geophysical
315 Research*, 69(20), 4377-4388, doi: DOI 10.1029/JZ069i020p04377.

316 Chigarev, N., P. Zinin, L. C. Ming, G. Amulele, A. Bulou, and V. Gusev (2008), Laser
317 generation and detection of longitudinal and shear acoustic waves in a diamond anvil cell, *Appl
318 Phys Lett*, 93(18), doi: 10.1063/1.3013587.

319 Davies, G. F., and A. M. Dziewonski (1975), Homogeneity and Constitution of Earths Lower
320 Mantle and Outer Core, *Physics of the Earth and Planetary Interiors*, 10(4), 336-343, doi: Doi
321 10.1016/0031-9201(75)90060-6.

322 Decremps, F., D. Antonangeli, M. Gauthier, S. Ayrinhac, M. Morand, G. L. Marchand, F.
323 Bergame, and J. Philippe (2014), Sound velocity of iron up to 152 GPa by picosecond acoustics
324 in diamond anvil cell, *Geophysical Research Letters*, 41(5), 1459-1464, doi:
325 10.1002/2013gl058859.

326 Dever, D. J. (1972), Temperature dependence of the elastic constants in α -iron single crystals:
327 relationship to spin order and diffusion anomalies, *Journal of Applied Physics*, 43(8), 3293-3301,
328 doi: 10.1063/1.1661710.

329 Dubrovinsky, L., et al. (2007), Body-centered cubic iron-nickel alloy in Earth's core, *Science*,
330 316(5833), 1880-1883, doi: 10.1126/science.1142105.

331 Dziewonski, A. M., and D. L. Anderson (1981), Preliminary Reference Earth Model, *Physics of
332 the Earth and Planetary Interiors*, 25(4), 297-356, doi: Doi 10.1016/0031-9201(81)90046-7.

333 Fiquet, G., J. Badro, F. Guyot, H. Requardt, and M. Krisch (2001), Sound velocities in iron to
334 110 gigapascals, *Science*, 291(5503), 468-471, doi: 10.1126/science.291.5503.468.

335 Gleason, A. E., W. L. Mao, and J. Y. Zhao (2013), Sound velocities for hexagonally close-
336 packed iron compressed hydrostatically to 136 GPa from phonon density of states, *Geophysical
337 Research Letters*, 40(12), 2983-2987, doi: 10.1002/grl.50588.

338 Huang, E., W. A. Bassett, and P. Tao (1987), Pressure-temperature-volume relationship for
339 hexagonal close packed iron determined by synchrotron radiation, *Journal of Geophysical
340 Research*, 92(B8), doi: 10.1029/JB092iB08p08129.

341 Huang, E., W. Bassett, and M. Weathers (1988), Phase relationships in Fe-Ni alloys at high
342 pressures and temperatures, *Journal of Geophysical Research*, 93(B7), doi:
343 10.1029/JB093iB07p07741.

344 Huang, E., W. A. Bassett, and M. S. Weathers (1992), Phase diagram and elastic properties of Fe
345 30% Ni alloy by synchrotron radiation, *Journal of Geophysical Research*, 97(B4), doi:
346 10.1029/92jb00020.

347 Isaak, D. G., and K. Masuda (1995), Elastic and viscoelastic properties of α iron at high
348 temperatures, *Journal of Geophysical Research: Solid Earth*, 100(B9), 17689-17698, doi:
349 10.1029/95jb01235.

350 Kantor, A. P., I. Y. Kantor, A. V. Kurnosov, A. Y. Kuznetsov, N. A. Dubrovinskaia, M. Krisch,
351 A. A. Bossak, V. P. Dmitriev, V. S. Urusov, and L. S. Dubrovinsky (2007), Sound wave
352 velocities of fcc Fe–Ni alloy at high pressure and temperature by mean of inelastic X-ray
353 scattering, *Physics of the Earth and Planetary Interiors*, 164(1-2), 83-89, doi:
354 10.1016/j.pepi.2007.06.006.

355 Li, B., and J. Zhang (2005), Pressure and temperature dependence of elastic wave velocity of
356 MgSiO_3 perovskite and the composition of the lower mantle, *Physics of the Earth and Planetary*
357 *Interiors*, 151(1-2), 143-154, doi: 10.1016/j.pepi.2005.02.004.

358 Li, B., R. C. Liebermann, and D. J. Weidner (2001), P-V-Vp-Vs-Tmeasurements on wadsleyite
359 to 7 GPa and 873 K: Implications for the 410-km seismic discontinuity, *Journal of Geophysical*
360 *Research: Solid Earth*, 106(B12), 30579-30591, doi: 10.1029/2001jb000317.

361 Li, B., J. Kung, and R. Liebermann (2004), Modern techniques in measuring elasticity of Earth
362 materials at high pressure and high temperature using ultrasonic interferometry in conjunction
363 with synchrotron X-radiation in multi-anvil apparatus, *Physics of the Earth and Planetary*
364 *Interiors*, 143-144, 559-574, doi: 10.1016/j.pepi.2003.09.020.

365 Li, B., K. Chen, J. Kung, R. Liebermann, and D. Weidner (2002), Sound velocity measurement
366 using transfer function method, *J Phys-Condens Mat*, 14(44), 11337-11342, doi: Pii S0953-
367 8984(02)38296-1 Doi 10.1088/0953-8984/14/44/478.

368 Li, J., and Y. Fei (2003), Experimental constraints on core composition, *Treatise on*
369 *geochemistry*, 2, 568.

370 Lin, J. F., W. Sturhahn, J. Y. Zhao, G. Y. Shen, H. K. Mao, and R. J. Hemley (2005), Sound
371 velocities of hot dense iron: Birch's law revisited, *Science*, 308(5730), 1892-1894, doi:
372 10.1126/science.1111724.

373 Lin, J. F., V. V. Struzhkin, W. Sturhahn, E. Huang, J. Zhao, M. Y. Hu, E. E. Alp, H. k. Mao, N.
374 Boctor, and R. J. Hemley (2003), Sound velocities of iron-nickel and iron-silicon alloys at high
375 pressures, *Geophysical Research Letters*, 30(21).

376 Liu, J., J. F. Lin, A. Alatas, and W. Bi (2014), Sound velocities of bcc-Fe and Fe0.85Si0.15 alloy
377 at high pressure and temperature, *Physics of the Earth and Planetary Interiors*, 233, 24-32, doi:
378 10.1016/j.pepi.2014.05.008.

379 Mao, H. K., Y. Wu, L. C. Chen, J. F. Shu, and A. P. Jephcoat (1990), Static compression of iron
380 to 300 GPa and Fe0.8Ni0.2alloy to 260 GPa: Implications for composition of the core, *Journal of*
381 *Geophysical Research*, 95(B13), doi: 10.1029/JB095iB13p21737.

382 Mao, H. K., J. F. Shu, G. Y. Shen, R. J. Hemley, B. S. Li, and A. K. Singh (1998), Elasticity and
383 rheology of iron above 220 GPa and the nature of the Earth's inner core, *Nature*, 396(6713), 741-
384 743, doi: Doi 10.1038/25506.

385 Mao, Z., J. F. Lin, J. Liu, A. Alatas, L. Gao, J. Zhao, and H. K. Mao (2012), Sound velocities of
386 Fe and Fe-Si alloy in the Earth's core, *Proc Natl Acad Sci U S A*, 109(26), 10239-10244, doi:
387 10.1073/pnas.1207086109.

388 Martorell, B., L. Vocadlo, J. Brodholt, and I. G. Wood (2013), Strong premelting effect in the
389 elastic properties of hcp-Fe under inner-core conditions, *Science*, 342(6157), 466-468, doi:
390 10.1126/science.1243651.

391 McDonough, W. F., and S. S. Sun (1995), The Composition of the Earth, *Chem Geol*, 120(3-4),
392 223-253, doi: Doi 10.1016/0009-2541(94)00140-4.

393 Morrison, R. A., J. M. Jackson, W. Sturhahn, D. Zhang, and E. Greenberg (2018), Equations of
394 State and Anisotropy of Fe-Ni-Si Alloys, *Journal of Geophysical Research: Solid Earth*, 123(6),
395 4647-4675, doi: 10.1029/2017jb015343.

396 Morrison, R. A., J. M. Jackson, W. Sturhahn, J. Zhao, and T. S. Toellner (2019), High pressure
397 thermoelasticity and sound velocities of Fe-Ni-Si alloys, *Physics of the Earth and Planetary
398 Interiors*, 294, doi: 10.1016/j.pepi.2019.05.011.

399 Murphy, C. A., J. M. Jackson, and W. Sturhahn (2013), Experimental constraints on the
400 thermodynamics and sound velocities of hcp-Fe to core pressures, *Journal of Geophysical
401 Research: Solid Earth*, 118(5), 1999-2016, doi: 10.1002/jgrb.50166.

402 Ohtani, E., Y. Shibasaki, T. Sakai, K. Mibe, H. Fukui, S. Kamada, T. Sakamaki, Y. Seto, S.
403 Tsutsui, and A. Q. R. Baron (2013), Sound velocity of hexagonal close-packed iron up to core
404 pressures, *Geophysical Research Letters*, 40(19), 5089-5094, doi: 10.1002/grl.50992.

405 Poirier, J.-P. (2000), *Introduction to the Physics of the Earth's Interior*, Cambridge University
406 Press.

407 Quarenici, F., and F. Mulargia (1988), The validity of the common approximate expressions for
408 the Grüneisen parameter, *Geophys J Int*, 93(3), 505-519.

409 Sakai, T., S. Takahashi, N. Nishitani, I. Mashino, E. Ohtani, and N. Hirao (2014), Equation of
410 state of pure iron and Fe0.9Ni0.1 alloy up to 3Mbar, *Physics of the Earth and Planetary Interiors*,
411 228, 114-126, doi: 10.1016/j.pepi.2013.12.010.

412 Shibasaki, Y., et al. (2016), Compressional and shear wave velocities for polycrystallinebcc-Fe
413 up to 6.3 GPa and 800 K, *American Mineralogist*, 101(5), 1150-1160, doi: 10.2138/am-2016-
414 5545.

415 Takahashi, T., W. A. Bassett, and H.-K. Mao (1968), Isothermal compression of the alloys of
416 iron up to 300 kilobars at room temperature: Iron-nickel alloys, *Journal of Geophysical Research*,
417 73(14), 4717-4725, doi: 10.1029/JB073i014p04717.

418 Tateno, S., K. Hirose, Y. Ohishi, and Y. Tatsumi (2010), The Structure of Iron in Earth's Inner
419 Core, *Science*, 330(6002), 359-361, doi: 10.1126/science.1194662.

420 Tateno, S., K. Hirose, T. Komabayashi, H. Ozawa, and Y. Ohishi (2012), The structure of Fe-Ni
421 alloy in Earth's inner core, *Geophysical Research Letters*, 39(12), doi: 10.1029/2012gl052103.

422 Vocadlo, L., D. Alfe, M. J. Gillan, I. G. Wood, J. P. Brodholt, and G. D. Price (2003), Possible
423 thermal and chemical stabilization of body-centred-cubic iron in the Earth's core, *Nature*,
424(6948), 536-539, doi: 10.1038/nature01829.

425 Wakamatsu, T., K. Ohta, T. Yagi, K. Hirose, and Y. Ohishi (2018), Measurements of sound
426 velocity in iron-nickel alloys by femtosecond laser pulses in a diamond anvil cell, *Phys Chem
427 Miner*, 45(6), 589-595, doi: 10.1007/s00269-018-0944-3.

428 Wang, X., T. Chen, X. Qi, Y. Zou, J. Kung, T. Yu, Y. Wang, R. C. Liebermann, and B. Li
429 (2015), Acoustic travel time gauges for in-situ determination of pressure and temperature in
430 multi-anvil apparatus, *Journal of Applied Physics*, 118(6), doi: 10.1063/1.4928147.

431 Zhang, J., and F. Guyot (1999), Thermal equation of state of iron and Fe 0.91 Si 0.09, *Phys
432 Chem Miner*, 26(3), 206-211.